# High-Frequency 4-Dimensional Ultrasound (4DUS): A Reliable Method for Assessing Murine Cardiac Function

**Frederick W. Damen[1], Alycia G. Berman[1], Arvin H. Soepriatna[1], Jessica M. Ellis[2], Stephen D. Buttars[3], Kristiina L. Aasa[3], and Craig J. Goergen[1]**

[1]Weldon School of Biomedical Engineering, Purdue University, West Lafayette, IN; [2]Department of Nutrition Science, Purdue University, West Lafayette, IN; and [3]FUJIFILM VisualSonics, Toronto, ON, Canada

**Corresponding Author:**
Craig J. Goergen, PhD
206 S. Martin Jischke Dr., West Lafayette, IN 47907, USA;
E-mail: cgoergen@purdue.edu

**Key Words:** ultrasound, cine MRI, cardiac disease, mouse, hypertrophy
**Abbreviations:** Short-axis motion-mode (SAX MM); magnetic resonance imaging (MRI); 4-dimensional ultrasound (4DUS); left ventricle (LV); end-diastole volume (EDV), peak-systole volume (PSV), stroke volume (SV), ejection fraction (EF), left ventricle mass (LVM)

ABSTRACT

In vivo imaging has provided a unique framework for studying pathological progression in various mouse models of cardiac disease. Although conventional short-axis motion-mode (SAX MM) ultrasound and cine magnetic resonance imaging (MRI) are two of the most prevalent strategies used for quantifying cardiac function, there are few notable limitations including imprecision, inaccuracy, and geometric assumptions with ultrasound, or large and costly systems with substantial infrastructure requirements with MRI. Here we present an automated 4-dimensional ultrasound (4DUS) technique that provides comparable information to cine MRI through spatiotemporally synced imaging of cardiac motion. Cardiac function metrics derived from SAX MM, cine MRI, and 4DUS data show close agreement between cine MRI and 4DUS but overestimations by SAX MM. The inclusion of a mouse model of cardiac hypertrophy further highlights the precision of 4DUS compared with that of SAX MM, with narrower groupings of cardiac metrics based on health status. Our findings suggest that murine 4DUS can be used as a reliable, accurate, and cost-effective technique for longitudinal studies of cardiac function and disease progression.

## INTRODUCTION

Murine cardiac disease models have become the foundation for systematically studying mechanisms and factors that influence negative outcomes such as heart failure (1-3). Although ex vivo techniques (eg, histology, proteomics) provide substantial information regarding gross and molecular composition, their information is limited to the state of tissue at sacrifice. In vivo imaging, on the other hand, can provide longitudinal information and result in a more comprehensive understanding of disease progression, particularly when studying changes in cardiac function. Although many noninvasive imaging modalities exist, high-frequency ultrasound and cine magnetic resonance imaging (MRI) are most widely used to assess murine cardiac function (4-6).

High-frequency ultrasound uses megahertz-frequency ultrasonic waves to acquire images of the heart, with contrast corresponding to differences in acoustic impedance between tissue types. This modality is particularly useful for imaging mice, as even with their rapid heart rates (approaching 600 bpm), near-real-time temporal resolution can be achieved. Nevertheless, standard ultrasound imaging techniques for calculating cardiac function (eg, short-axis motion-mode or M-Mode [SAX MM]) require the use of geometric models to estimate the ventricular volumes as spheres, ellipsoids, or other shapes (7, 8). Although these geometric assumptions are commonly used to study heart function in vivo (9, 10), the left ventricle (LV) in a mouse has a complicated 3-dimensional shape, which can increase in complexity with varying disease states.

Cardiac cine MRI exploits the contrasting magnetic properties of myocardial tissue and flowing blood to collect volumetric information across a heartbeat. These 4-dimesional (3-dimensional + time) data are spatiotemporally compiled from spatially adjacent slices of cine data across the heart. Compared with ultrasound, cine MRI takes longer to process images because the region of interest must be sampled several times before each slice of cine data can be properly reconstructed. However, cine MRI is often considered a gold standard method for acquiring LV information, as the chamber's entire boundary can be directly imaged (11-13). Unfortunately, acquiring cine MRI data is often costlier owing to system availability, maintenance, and required infrastructure for operating a superconducting magnet.

Building upon the idea of spatiotemporally compiling loops of MRI data, we present here an automated 4D ultrasound (4DUS)


ISSN 2379-1381 http://dx.doi.org/10.18383/j.tom.2017.00016

technique that can provide comparable information free of heuristics. We compared this technique against conventional SAX MM and cine MRI by using cardiac function metrics to assess their relative performance. The results of this murine study suggest that cardiac 4DUS has advantages over standard 2D techniques and can be used as an alternative to cine MRI.

## METHODOLOGY

### Murine Models

In total, 10 female mice were used in this study. All mice were bred at Purdue University and derived from *Cpt2*-floxed mice crossed with Cre-expressing mice, in which Cre was driven by the muscle creatine kinase promoter [Stock No: 006475; Jackson Laboratories, Bar Harbor, ME, USA; (14, 15)]. Mice deficient in cardiac Cpt2 ($Cpt2^{M-/-}$; n = 5; age = 11.2 weeks; body mass = 20.1 [0.71] g), hereafter referred to as the $Cpt2^{M-/-}$ cohort, have impaired cardiomyocyte fatty acid oxidative metabolism owing to compromised transport of long-chain fatty acids into the mitochondria through acyl-carnitine-mediated transport (14). Our previous work showed that the loss of cardiac Cpt2 results in left ventricular hypertrophy (15). Control mice, hereafter referred to as the wild-type cohort, were littermates lacking the Cre gene ($Cpt2^{flox/flox}$; n = 5; age = 11.2 weeks; body mass = 19.5 [0.57] g). All animal experiments were approved by the Purdue Animal Care and Use Committee.

### Magnetic Resonance Imaging

Cardiac MRI data were compiled for each mouse from adjacent short-axis cine loops across the LV by using a small-bore 7 T MRI system (BioSpec 70/30 USR, Bruker Corporation, Billerica, MA). A circularly polarized transmit/receive $^1$H volume coil was used in combination with a retrospectively gated Fast Low-Angle SHot (IntraGateFLASH) sequence with in-slice navigator (16, 17) with repetition time/echo time = 7/3 milliseconds; flip angle = 20°; slice thickness = 1.0 mm, cine frames = 14, matrix size = $256^2$, NEX = 1, field of view = 35 × 25 mm, and pixel size = 137 × 98 $\mu$m. To help position sequential short-axis slices, a 4-chamber long-axis view of the heart was acquired with similar parameters. Short-axis slices were prescribed, ensuring coverage from the apex to the ascending aorta. Magnitude cine data were extracted and spatiotemporally concatenated into 4D data using MATLAB (MathWorks, Natick, MA). Figure 1C shows representative magnetic resonance data at end-diastole with axial, sagittal, and coronal slices through the center of the LV.

### High-Frequency Ultrasound: 4DUS and SAX MM

4DUS and SAX MM data were acquired using a high-frequency small animal ultrasound system (Vevo 3100, FUJIFILM VisualSonics Inc., Toronto, ON, Canada) and a 40-MHz center frequency linear array transducer (MX550D, FUJIFILM VisualSonics Inc.). In preparation for ultrasound imaging, depilatory cream was applied to the ventral thorax to prevent hair-based artifacts. The ultrasound probe was clamped to a linearly translating step motor and positioned parallel to the short axis of the LV. System-integrated triggering between the probe and motor automatically acquired a high frame rate (300 fps) cardiac- and respiratory-gated cine loops and spatiotemporally compiled them into 4D data. A volumetric field of view was prescribed to ensure that the end-diastolic epicardium would fit in all frames, spanning from the apex to the aortic valve. The axial and lateral pixel sizes were set at 12.0 × 55.2 $\mu$m (axial resolution = 40 $\mu$m; lateral resolution = 90 $\mu$m), with a step-size of 76.2 $\mu$m. Figure 1B shows a representative example of 4DUS data at end-diastole, with axial, sagittal, and coronal slices through the center of the LV, similar to the magnetic resonance data display.

Following 4D data collection, the probe was positioned midpapillary with a short-axis orientation. A line and cursor defining the SAX MM data were prescribed down the center of the ventricle, and ~5 seconds of data were acquired. Figure 1A shows a representation of the prescribed cursor and corresponding SAX MM data.

### Anesthesia and Physiological Monitoring

Mice were anesthetized during each imaging procedure using a low-flow vaporizer (SomnoSuite, Kent Scientific, Torrington, CT) with ~2.5% isoflurane at 250 mL/min (18). The exact anesthetic level was modulated as needed to maintain a heart rate near 500 beats/min and respiration rate near 60 breaths/min. During MRI, heart rate and respiration were monitored by means of 3 subcutaneous needle electrodes and a pneumatic pillow pressure sensor, respectively (SA Instruments, Stony Brook, NY). Furthermore, each animal was maintained at 37°C by using a feedback-modulated fan that blew heated air into the bore of the magnet. During ultrasound imaging, a heated stage with integrated gold-plated electrodes (Vevo Imaging Station, FUJIFILM VisualSonics Inc.) warmed the animal to a temperature of approximately 37°C while also obtaining heart rate and respiratory signals. Respiratory signals were simultaneously extracted from gold-plated electrodes by filtering low-frequency signal fluctuations, caused by changes in impedance across the lungs during inhalation. Rectal temperature probes were used to monitor core body temperature with both imaging systems.

### Cardiac Function Assessment

Using a custom MATLAB GUI and Vevo 3100 compatible VevoLAB analysis software (v3.0) for the MRI and 4DUS data, respectively, the endocardial and epicardial borders of the LV were manually outlined across short-axis views of the heart. The endocardial border was used to define the LV chamber, and the endocardial and epicardial borders were used in conjunction to define the LV myocardium. Maintaining conventions set by the American Society of Echocardiography (9, 10), the proximal extent of the LV cavity was defined as the mitral and aortic valves, and the papillary muscles were considered part of the LV cavity. These guidelines were followed across all animals, regardless of gross differences in heart size or shape. Figure 2, A and B illustrates an example of the aforementioned border definitions.

Expediting mask creation in the 4DUS data, we manually outlined slices that were ~0.3–0.5 mm (ie, 4–6 slices) apart and we then used cubic spline interpolation to fill in the boundaries over skipped regions (Figure 2C; middle). To ensure that using such interpolation will not produce large deviations from the expected ground truth, a sensitivity analysis was performed; LV mask volumes were compared over a series of gap sizes and

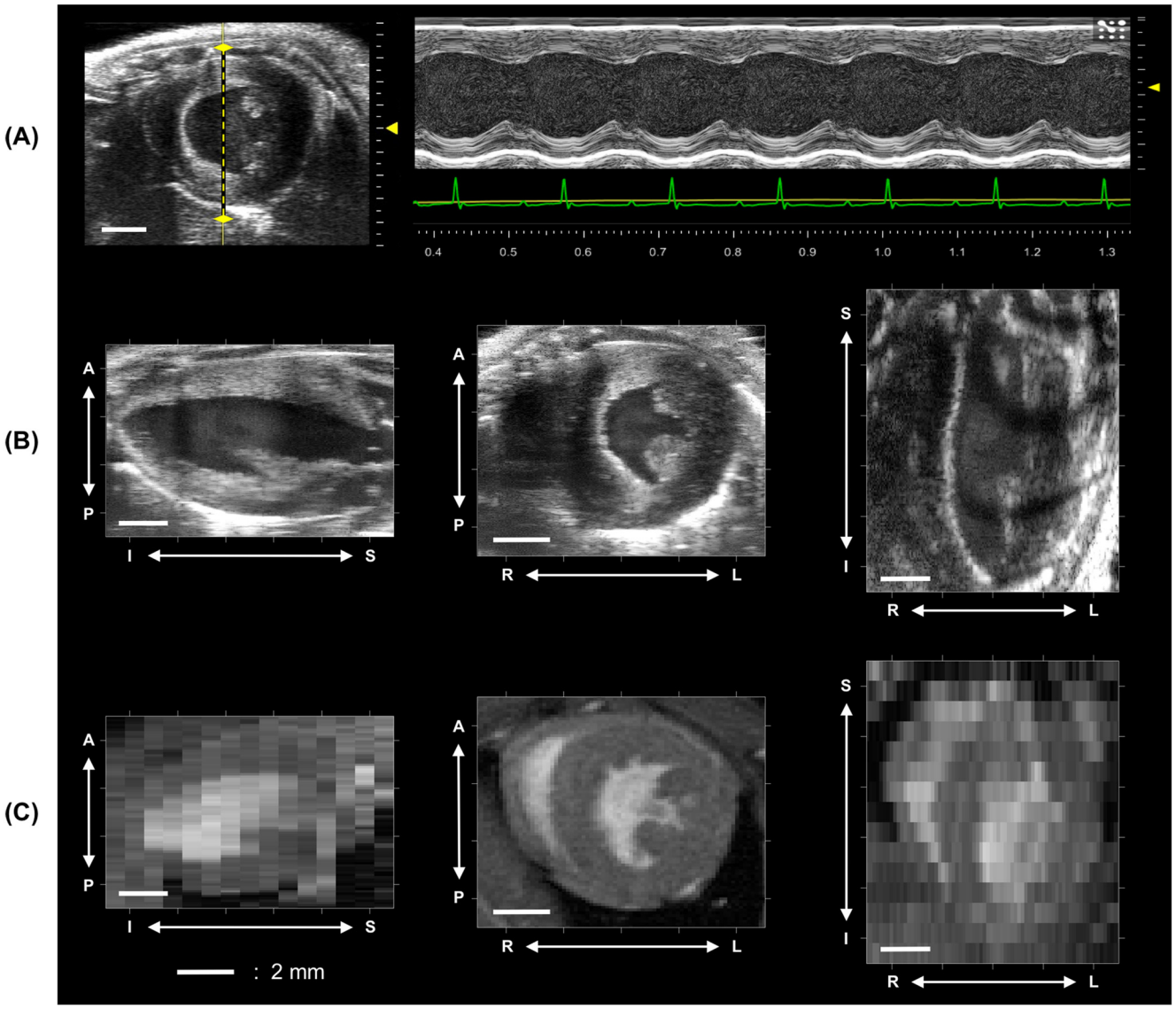


**Figure 1.** Representative displays of the imaging modalities used on an example mouse: short-axis M-Mode (SAX MM) (A), 4D ultrasound (4DUS) (B), and bright-blood gradient echo magnetic resonance imaging (MRI) (C). The SAX MM row shows the prescribed cursor for sampling (dashed yellow line) along with corresponding data time-synced to ECG signals. Both 4DUS and MRI rows show long-axis (left), short-axis (center), and 4-chamber (right) views at corresponding slice locations (scale bar = 2.0 mm).

position paradigms. Figure 2C shows an example cross-sectional area profile for a mask without any gaps (ie, complete masking) and for 2 subsequent gap paradigms. Quantifying the percent difference in the volume of every gap paradigm from the complete masking, Figure 2D shows the results of sensitivity analysis for an example wild-type, early-stage disease, and late-stage disease mouse. We observed that gap sizes approximately ≤0.5 mm did not produce percent differences in mask volumes >1%, thus providing us confidence in the reliability of our masking protocol.

To extract measurements from the SAX MM data, the VevoLAB software was used to draw lines corresponding to the endocardial and epicardial borders through at least 3 cardiac cycles. Estimates of left ventricular geometry were thus calculated using the mean of corresponding measurements at end-diastole and peak-systole (ie, maximum and minimum distances between endocardial borders). A single reviewer performed all measurements to prevent interoperator variability.

Ventricular chamber volumes defined by the endocardial border from MRI and 4DUS data measured at end-diastole volume (EDV) and peak-systole volume (PSV) were used to calculate the LV stroke volume (SV) and ejection fraction (EF). To estimate the mass of the LV myocardium (ie, left ventricle mass [LVM]), EDV was subtracted from the total volume defined by the epicardial border at EDV (EpiEDV), and the resultant volume

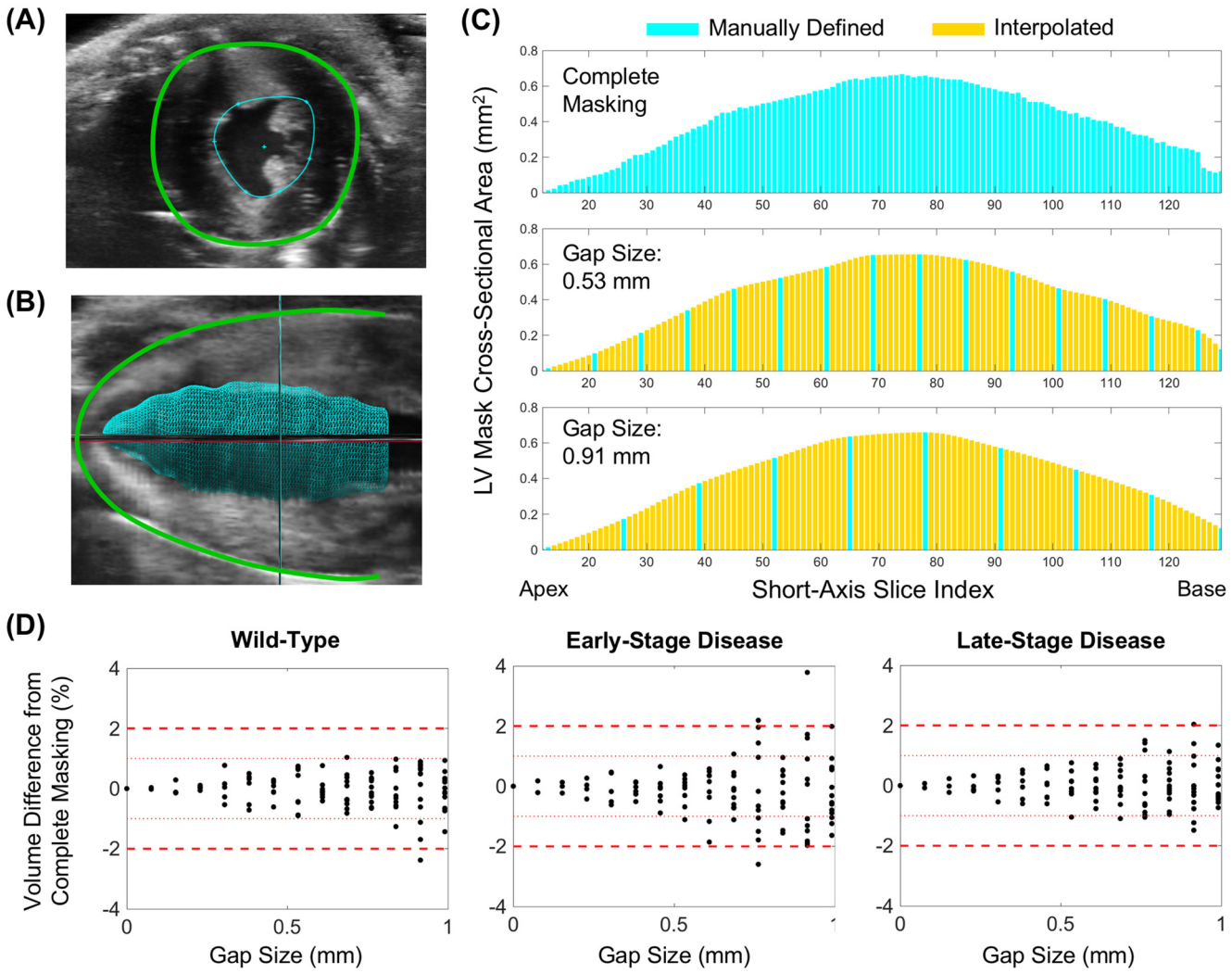


**Figure 2.** Overview of masking and slice analysis. Example short-axis 4DUS slices with outlines of endocardial (blue) and epicardial (green) borders drawn (A). Adjacent short-axis border definitions are pieced together to create a volumetric mask, as shown in (B) with an example mask (blue) of the left ventricle (LV) in a long-axis view. The epicardial border (green) was also included in (B) for reference. To identify the sensitivity of total mask volume to interpolated borders across skipped slices, a complete masking (ie, every slice across the volume was manually outlined) had equal-sized subsets of slices deleted (C; top), which were subsequently filled using cubic spline interpolation (C; middle/bottom). A slice thickness of 0.0762 mm was used to calculate physical gap sizes. At each gap size, the set of remaining slices—excluding the most proximal and distal slices—were serially shifted to identify variability based on gap positioning. Total volumes were calculated for each paradigm as the sum of all cross-sectional areas. Percent differences in volume from the complete masking across all gap paradigms are shown for a representative wild-type (D; left), early-stage disease (D; middle), and late-stage disease mouse (D; right).

multiplied by a cardiac tissue density of 1.05 mg/$\mu$L (19, 20). The equations used to calculate cardiac function include:

$$EF = (EDV - PSV) / EDV \times 100$$
$$SV = EDV - PSV$$
$$LVM = 1.05 \times (EpiEDV - EDV)$$

In contrast to direct measurements from the volumetric data, the M-Mode analysis used the Teichholz equation to quantify the LV volume (LVV), as follows:

$$LVV = (7.0 / (2.4 + LVID)) \times LVID^3$$

Where left ventricular inner diameter (LVID) is used to estimate the geometry of the ventricle at any corresponding point in the cardiac cycle (21). These estimated EDV and PSV values were incorporated into the same equations as above to calculate EF and SV. Calculations of LVM on the basis of M-Mode data incorporated the measured thickness of the LV anterior wall (LVAW) and LV posterior wall (LVPW), as shown in the following equation:

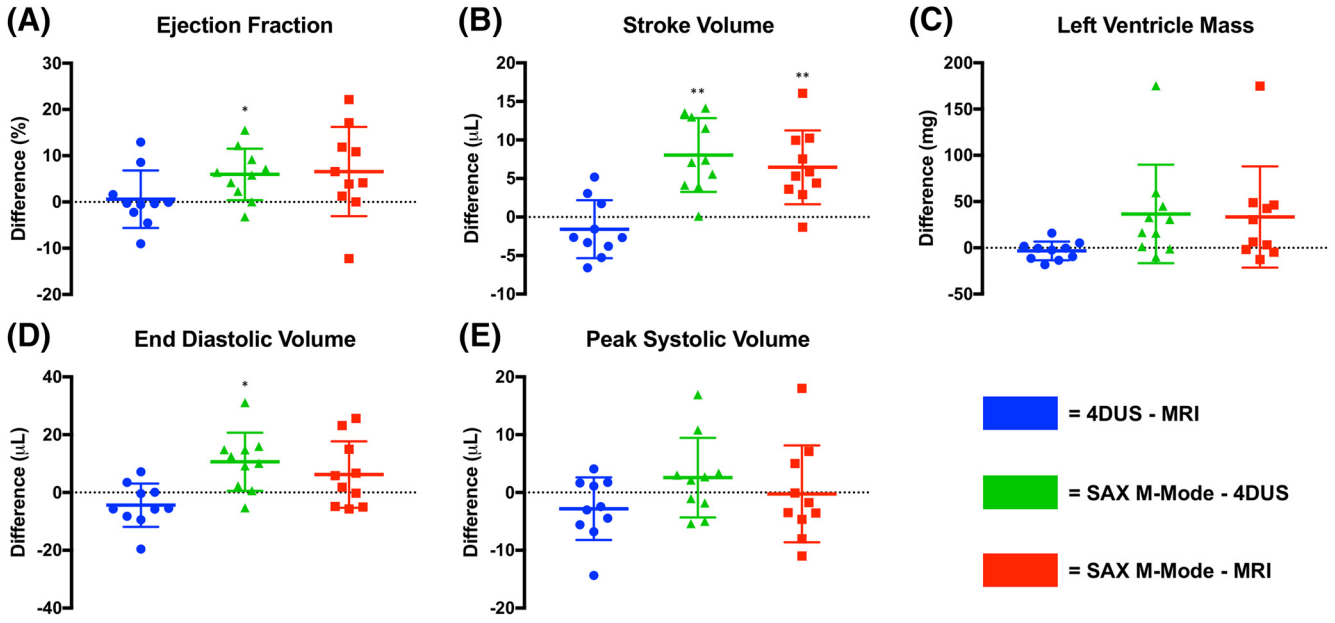


**Figure 3.** Scatter dot plots with mean and standard deviation bars comparing measurement differences between each pair of imaging methods. In each plot, the left blue column represents the 4DUS–MRI values, the green center column represents the SAX MM–4DUS values, and the red right column represents the SAX MM–MRI values. The plots of ejection fraction (A), stroke volume (B), and LV mass (C) each represent metrics derived from volume estimates made at end-diastole (D) and peak-systole (E), commonly used to evaluate left ventricular function. One-way ANOVA identified statistical significance between methods as designated by $*P < .05$ and $**P < .01$, respectively.

$$\text{LVM} = 1.05 \times [(\text{LVID} + \text{LVAW} + \text{LVPW})^3 - \text{LVID}^3] \times 0.8$$

### Histology

Following imaging, mice were euthanized with $CO_2$ overdose and cervical dislocation. Hearts were excised and then placed directly in 4.0% paraformaldehyde and stored at 4°C. After 6 days, hearts were transferred to 0.1% paraformaldehyde and again stored at 4°C until histology was performed. Each heart was embedded in paraffin and sectioned along the midpapillary short axis of the LV. Tissue sections were stained with H&E and Masson's Trichrome following standard protocols.

### Statistical Analysis

Differences between imaging methods were assessed in scatter dot plots. A 1-way ANOVA with multiple comparisons was performed to identify significant differences between each pairing of methods. To compare cardiac function metrics between the 3 methods and 2 groups of mice (ie, wild-type and $Cpt2^{M-/-}$), 2-way ANOVA with Tukey corrections for multiple comparisons was performed.

## RESULTS AND DISCUSSION

The present study introduces an automated 4DUS technique and compares its performance in assessing cardiac function with that of conventionally used SAX MM and MRI methods. Quantified metrics of cardiac function (ie, EDV, PSV, EF, SV, and LVM) from each of the 3 aforementioned techniques, acquired on each subject, were the basis for comparison. The 4DUS and MRI methods did not produce significant differences in any of the used metrics, whereas the SAX MM overestimated these values on average (Figure 3). The 1-way ANOVA indicated a significantly larger EF obtained from SAX MM than from 4DUS ($P = .020$), larger SV from SAX MM than from both 4DUS ($P = .001$) and MRI methods ($P = .005$), and larger EDV from SAX MM than from 4DUS ($P = .021$). Because cine MRI data are widely accepted as a gold standard in measuring chamber volumes, our findings suggest that 4DUS could be a reliable alternative to cine MRI. Furthermore, as 4DUS and MRI do not rely on simplified models of LV geometries, these results provide further evidence that the geometric models used in SAX MM could be a source of inaccuracy in assessing cardiac function (8-10).

Subsequent analysis compared method performance taking into account cohort classifications (ie, wild-type or $Cpt2^{M-/-}$). Table 1 shows metric averages separated by cohort and identifies significant differences following a 2-way ANOVA, which incorporated both imaging modality and cohort as factors. Neither wild-type nor diseased mice showed any significant difference between the 4DUS and MRI techniques, similar to the results of our initial 1-way ANOVA analysis. However, significantly larger values were observed for SAX MM versus MRI methods in (1) the wild-type group for EDV ($P = .014$) and SV ($P = .002$) and in (2) the diseased group for EF ($P = .02$) and LVM ($P = .002$). Furthermore, the SAX MM had significantly larger values than the 4DUS methods in (1) the wild-type group

**Table 1.** Average Values for All Measured and Calculated Metrics, Divided by Wild-type (A) and Cpt2$^{M-/-}$ (B) Cohorts

| | Wild-Type Mice | | | | |
|---|---|---|---|---|---|
| **(A)** | **EDV (μL)** | **PSV (μL)** | **EF (%)** | **SV (μL)** | **LVM (mg)** |
| SAX MM | 51.1 (14.4)*,+ | 20.2 (9.4) | 62.0 (8.5) | 30.9 (6.2)**,+++ | 73.7 (9.6) |
| MRI | 38.2 (3.1) | 15.8 (1.6) | 58.6 (3.1) | 22.4 (2.3) | 75.6 (8.4) |
| 4DUS | 38.1 (5.8) | 16.9 (2.8) | 55.7 (2.1) | 21.2 (3.2) | 69.2 (3.0) |
| | **CPT2$^{M-/-}$ Mice** | | | | |
| **(B)** | **EDV (μL)** | **PSV (μL)** | **EF (%)** | **SV (μL)** | **LVM (mg)** |
| SAX MM | 61.2 (26.3) | 30.7 (26.6) | 56.1 (18.9)* | 30.4 (4.7)+ | 235.5 (89.9)**,++ |
| MRI | 61.6 (27.5) | 35.6 (25.1) | 46.4 (12.3) | 26.0 (3.9) | 166.9 (39.7) |
| 4DUS | 52.9 (21.6) | 28.9 (21.4) | 50.5 (15.9) | 24.0 (2.0) | 166.7 (33.1) |

The metrics shown are end-diastolic volume (EDV), peak-systolic volume (PSV), ejection fraction (EF), stroke volume (SV), and left ventricle mass (LVM). Two-way ANOVA analysis with Tukey post-hoc comparisons was performed on the shown data. Significant within-group differences are designated with * symbols for SAX MM versus MRI values and + symbols for SAX MM versus 4DUS values, as well as 1, 2, or 3 symbol repetitions for significance levels of $P < .05$, $P < .01$, and $P = .001$, respectively. No significant differences were found between the 4DUS and MRI values for any metrics.

for EDV ($P = .013$) and SV ($P = .001$) and in (2) the diseased group for SV ($P = .014$) and LVM ($P = .002$). The only insignificant interaction between imaging method and cohort was for LVM ($P = .116$); however, this is most likely because of the large overestimation by SAX MM in the Cpt2$^{M-/-}$ cohort. Interestingly, SAX MM overestimated EDV in our wild-type mice, but the differences in LVM measurements were not significant; an opposite trend was observed in the Cpt2$^{M-/-}$ group. We originally hypothesized that if either SAX MM metric (ie, EDV or LVM) would be inaccurate, it would be when cardiac morphology deviated from the wild-type state. Instead, the observed overestimation of LVM in the wild-type cohort suggests that the wild-type murine myocardium may be smaller than assumed in the used geometric models. Conversely, future use of SAX MM in murine models may consider refinement of the equations used to calculate the presented metrics, to better match the morphology of the murine heart.

Although we have so far focused on the agreement between each imaging modality, the use of *Cpt2$^{M-/-}$* mice also shows the benefit of acquiring reliable function metrics toward characterizing cardiac remodeling and the ultimate progression to heart failure. As observed in recent literature, this mouse model develops early concentric hypertrophy of the LV followed by chamber dilation (15). Representative histology (Figure 4) confirms the

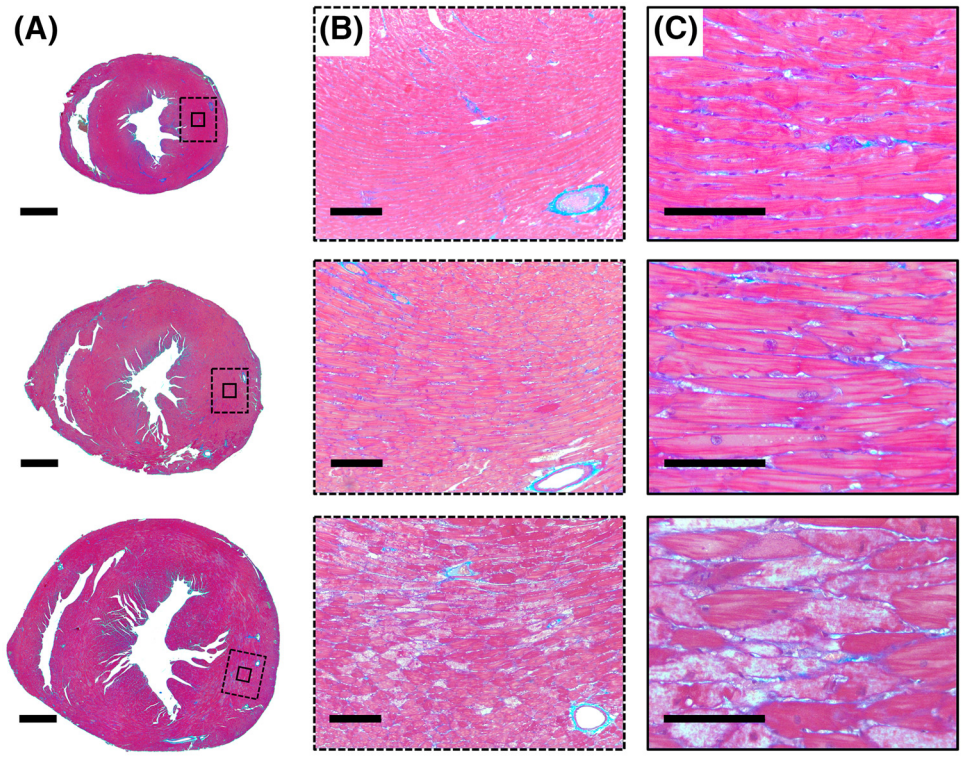


**Figure 4.** Representative Masson's Trichrome histology of the various disease stages imaged, with magnifications at 4× (scale bar = 1.0 mm) (A), 10× (scale bar = 200 μm) (B), and 40× (scale bar = 100 μm) (C). The first row shows a representative nonmutated mouse (n = 5), in which wild-type cardiomyocyte size and density are observed. The second row shows an early stage of hypertrophy (n = 3), in which enlarged cardiomyocytes are observed without any noticeable necrosis. The third row shows a late stage of hypertrophy (n = 2), in which enlarged cardiomyocytes and cell necrosis with less stain uptake are both observed.

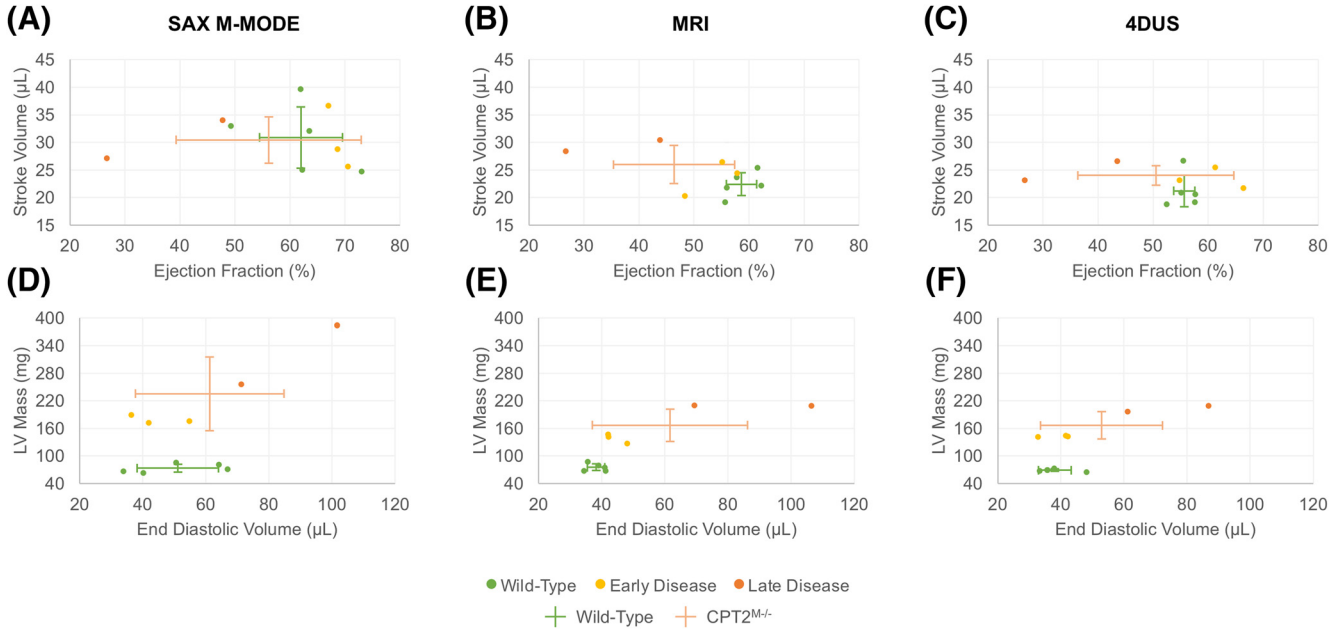


**Figure 5.** Characterization plots of the wild-type, early-stage disease, and late-stage disease mice derived from the 4DUS-based metrics. The top 3 plots of EF versus SV for SAX MM (A), MRI (B), and 4DUS (C) illustrate the relative spread of cardiac function metrics across the study animals. It is clear that the distributions are more closely matched for the MRI and 4DUS techniques. This agreement in metric distributions in also observed for the structural metrics of EDV versus LVM (D–F). The characteristics expected for the *CPT2*$^{M-/-}$ model are highlighted in these plots showing relative clusters depending on health status.

presence of both late (n = 2) and early (n = 3) stages of the disease within the Cpt2$^{M-/-}$ cohort, characterized by gross cardiomyocyte hypertrophy with or without notable cardiomyocyte necrosis (ie, hypereosinophilia and loss of cross striations), respectively. Plots of EF versus SV and EDV versus LVM (Figure 5) illustrate how both the wild-type and diseased cohorts can be characterized by physiologic- or morphologic-oriented metrics, respectively. In plots of EF versus SV, we note that while the stroke volume is relatively conserved for all mice, only early-stage-disease mice preserve an EF comparable to wild-type mice. In plots of EDV versus SV, both metrics seem to gradually increase with the relative stage of disease, illustrating somewhat distinct groupings based on the wild-type, *Cpt2*$^{M-/-}$ phenotype with early-stage disease, and *Cpt2*$^{M-/-}$ phenotype with late-stage disease. To demonstrate these groupings, data were displayed as both individual points and average distributions for the wild-type and Cpt2$^{M-/-}$ cohorts. These plots qualitatively exhibit the method agreement between MRI and 4DUS methods that have been quantitatively studied above.

Despite the advantages of 4DUS including rapid acquisition (eg, 5–10 min for 4DUS, <1 min for SAX MM, and 45–60 min for cine MRI), relatively low cost, and high spatiotemporal resolution, this approach does have several limitations compared with cine MRI. First, sternum, rib, and lung artifacts limit the imaging window and can obscure portions of the heart. This can be particularly difficult if interested in right ventricular pathologies, as the sternum artifact can blur a large portion of its endocardial borders. Second, similar to cine MRI, accurate ECG and respiration signals are required to spatiotemporally compile the 4DUS images. To this end, pathologies that include cardiac arrhythmias will need to be tested to ensure proper spatiotemporal compilation. Third, the higher spatial and temporal resolution of 4DUS information comparably increases the digital size of the data. Although most commonly available computational resources can handle such data sizes for analysis, down-sampling in the spatial and/or temporal domain can serve to reduce computational costs if desired.

In conclusion, we show in this study that 4DUS can provide data that are comparable to cine MRI for quantifying cardiac function metrics, with improved precision and accuracy over SAX MM ultrasound. Nevertheless, SAX MM is used widely as a relatively rapid and economical option for longitudinal studies of cardiac disease in murine studies (4, 5). Fortunately, the benefits of ultrasound and volumetric acquisition can be combined with only a slightly longer scan time compared with SAX MM. Using 4DUS imaging, rapid assessments with high-frequency ultrasound can be conducted with the crucial advantage of producing reliable measurements similar to the gold standard of cardiac MRI without assuming an idealized geometric model. Furthermore, the added benefit of higher through-plane resolution compared with MRI may help provide clearer data for studying cardiac disease models in which the myocardium evolves into even more complex

shapes (eg, myocardial infarction). While the $Cpt2^{M-/-}$ model used in this study exhibited global hypertrophy, the demonstrated performance of 4DUS was nevertheless valuable when quantifying ventricular size and function.

## ACKNOWLEDGMENTS

We would like to acknowledge Brett Hawkins and Andrew Needles from FUJIFILM VisualSonics for their assistance with this study. Frederick Damen was supported by the National Institutes of Health (NIH) NIDDK T32 Fellowship (DK101001-01). Alycia Berman was supported by the National Science Foundation through a Graduate Research Fellowship (DGE-1333468). This publication was made possible with support from the Indiana Clinical and Translational Sciences Institute funded, in part, by Award Number UL1TR001108 from the NIH, National Center for Advancing Translational Sciences, Clinical and Translational Sciences Award. The content is solely the responsibility of the authors and does not necessarily represent the official views of the NIH. Stephen Buttars and Kristiina Aasa are employees of FUJIFILM VisualSonics Inc.

## REFERENCES

1. Sheikh F, Chen J. Mouse models for cardiomyopathy research. Prog Pediatr Cardiol. 2007;24(1):27–34.
2. Patten RD, Hall-Porter MR. Small animal models of heart failure: development of novel therapies, past and present. Circ Heart Fail. 2009;2(2):138–144.
3. Zaragoza C, Gomez-Guerrero C, Martin-Ventura JL, Blanco-Colio L, Lavin B, Mallavia B, Tarin C, Mas S, Ortiz A, Egido J. Animal models of cardiovascular diseases. J Biomed Biotechnol. 2011;2011:497841.
4. Gardin JM, Siri FM, Kitsis RN, Edwards JG, Leinwand LA. Echocardiographic assessment of left ventricular mass and systolic function in mice. Circ Res. 1995; 76(5):907–914.
5. Pistner A, Belmonte S, Coulthard T, Blaxall B. Murine echocardiography and ultrasound imaging. J Vis Exp. 2010(42). pii: 2100.
6. Akki A, Gupta A, Weiss RG. Magnetic resonance imaging and spectroscopy of the murine cardiovascular system. Am J Physiol Heart Circ Physiol. 2013;304(5): H633–H648.
7. Folland ED, Parisi AF, Moynihan PF, Jones DR, Feldman CL, Tow DE. Assessment of left ventricular ejection fraction and volumes by real-time, two-dimensional echocardiography. A comparison of cineangiographic and radionuclide techniques. Circulation. 1979;60(4):760–766.
8. Schiller NB, Foster E. Analysis of left ventricular systolic function. Heart. 1996; 75(6 Suppl 2):17–26.
9. Lang RM, Badano LP, Mor-Avi V, Afilalo J, Armstrong A, Ernande L, Flachskampf FA, Foster E, Goldstein SA, Kuznetsova T, Lancellotti P, Muraru D, Picard MH11, Rietzschel ER, Rudski L, Spencer KT, Tsang W, Voigt JU. Recommendations for cardiac chamber quantification by echocardiography in adults: an update from the American Society of Echocardiography and the European Association of Cardiovascular Imaging. J Am Soc Echocardiogr. 2015;28(1):1–39.e14.
10. Lang RM, Bierig M, Devereux RB, Flachskampf FA, Foster E, Pellikka PA, Picard MH, Roman MJ, Seward J, Shanewise J, Solomon S, Spencer KT, St John Sutton M, Stewart W. Recommendations for chamber quantification: A report from the American Society of Echocardiography's guidelines and standards committee and the chamber quantification writing group, developed in conjunction with the European Association of Echocardiography, a branch of the European Society of Cardiology. J Am Soc Echocardiogr. 2005;18(12):1440–1463.
11. Nahrendorf M, Hiller KH, Hu K, Ertl G, Haase A, Bauer WR. Cardiac magnetic resonance imaging in small animal models of human heart failure. Med Image Anal. 2003;7(3):369–375.
12. Franco F, Dubois SK, Peshock RM, Shohet RV. Magnetic resonance imaging accurately estimates LV mass in a transgenic mouse model of cardiac hypertrophy. Am J Physiol. 1998;274(2 Pt 2):H679–H683.
13. Wiesmann F, Ruff J, Hiller KH, Rommel E, Haase A, Neubauer S. Developmental changes of cardiac function and mass assessed with MRI in neonatal, juvenile, and adult mice. Am J Physiol Heart Circ Physiol. 2000;278(2):H652–H657.
14. Lee J, Ellis JM, Wolfgang MJ. Adipose fatty acid oxidation is required for thermogenesis and potentiates oxidative stress-induced inflammation. Cell Rep. 2015; 10(2):266–279.
15. Pereyra AS, Hasek LY, Harris KL, Berman AG, Damen FW, Goergen CJ, Ellis JM. Loss of cardiac carnitine palmitoyltransferase 2 results in rapamycin-resistant, acetylation-independent hypertrophy. J Biol Chem. 2017. [Epub ahead of print].
16. Bovens SM, te Boekhorst BC, den Ouden K, van de Kolk KW, Nauerth A, Nederhoff MG, Pasterkamp G, ten Hove M, van Echteld CJ. Evaluation of infarcted murine heart function: comparison of prospectively triggered with self-gated MRI. NMR Biomed. 2011;24(3):307–315.
17. Heijman E, de Graaf W, Niessen P, Nauerth A, van Eys G, de Graaf L, Nicolay K, Strijkers GJ. Comparison between prospective and retrospective triggering for mouse cardiac MRI. NMR Biomed. 2007;20(4):439–447.
18. Damen FW, Adelsperger AR, Wilson KE, Goergen CJ. Comparison of traditional and integrated digital anesthetic vaporizers. J Am Assoc Lab Anim Sci. 2015; 54(6):756–762.
19. Vinnakota KC, Bassingthwaighte JB. Myocardial density and composition: a basis for calculating intracellular metabolite concentrations. Am J Physiol Heart Circ Physiol. 2004;286(5):H1742–H1749.
20. Gao S, Ho D, Vatner DE, Vatner SF. Echocardiography in Mice. Curr Protoc Mouse Biol. 2011;1:71–83.
21. Teichholz LE, Kreulen T, Herman MV, Gorlin R. Problems in echocardiographic volume determinations: echocardiographic-angiographic correlations in the presence of absence of asynergy. Am J Cardiol. 1976;37(1):7–11.